Fermi National Accelerator Laboratory

FERMILAB-Pub-82/41-EXP
7170.272
7160.629
(Submitted to Nucl. Instrum. Methods)

OPERATIONAL PERFORMANCE OF A LARGE LIQUID ARGON PHOTON CALORIMETER

C. Nelson, J. Biel, T. Droege, A. Jonckheere, and P. Koehler
Fermi National Accelerator Laboratory, Batavia, Illinois 60510

and

D. Berg, C. Chandlee, S. Cihangir, T. Ferbel, J. Huston, T. Jensen,
J. LeBritton, F. Lobkowicz, M. McLaughlin, T. Ohshima,
P. Slattery, and P. Thompson
University of Rochester, Rochester, New York 14627

and

C. Bromberg and S. R. W. Cooper
Michigan State University, East Lansing, Michigan 48824

and

B. Collick, S. Heppelmann, Y. Makdisi, M. Marshak, E. Peterson,
J. Povlis, and K. Ruddick
University of Minnesota, Minneapolis, Minnesota 55455

and

B. Brown, D. Garelick, G. Glass, M. Glaubman, S. R. Han, and E. Pothier
Northeastern University, Boston, Massachusetts 02115

June 1982

Operational Performance of a Large Liquid Argon Photon Calorimeter

C. Nelson, J. Biel, T. Droege, A. Jonckheere and P. Koehler
Fermilab
Batavia, Il 60510

D. Berg, C. Chandlee, S. Cihangir, T. Ferbel, J. Huston, T. Jensen[†], J. LeBritton[††], F. Lobkowicz, M. McLaughlin, T. Ohshima[#], P. Slattery and P. Thompson*
University of Rochester
Rochester, N.Y. 14627

C. Bromberg and S. R. W. Cooper
Michigan State University
East Lansing, MI 48824

B. Collick, S. Heppelmann, Y. Makdisi*, M. Marshak, E. Peterson, J. Povlis
and K. Ruddick
University of Minnesota
Minneapolis, MN 55455

B. Brown, D. Garelick, G. Glass**, M. Glaubman, S. R. Han, E. Pothier
Northeastern University
Boston, MA 02115

[†] Presently at EP Division, CERN, 1211 Geneva 23, Switzerland.

[††] Presently at University of Arizona, Tucson, AZ 85721.

[#] Presently at INS, University of Tokyo, Tanashi City, Tokyo 188.

* Presently at BNL, Upton, N.Y. 11973.

** Visitor from Texas A&M University.

ABSTRACT

We describe the performance of a large (0.9 × 1.4 m^2) liquid argon photon calorimeter in high energy experiments at Fermilab. Resolutions for π^0 and electron showers, obtained under data-taking conditions, are compared with electron-beam calibration results. Exceptional spatial and time resolutions have been achieved for isolated showers ($\sigma_{x,y} < 0.7$ mm and $\sigma_t \simeq 6$ nsec). Electron data up to energies of 80 GeV and π^0 data up to 180 GeV are presented.

I. Introduction

Since their introduction into high energy physics[1], liquid argon calorimeters have proven to be exceedingly versatile detectors of electrons, photons and hadrons. The theory of operation and the design details of these detectors, and their cryogenic support systems, have been amply described[2].

In this paper we will present a summary of our operating experience with a large (0.9x1.4 m^2) photon calorimeter. Section II provides a brief discussion of the detector construction and Section III describes the readout electronics. In Section IV event reconstruction is discussed. In Section V we present results from electron-beam tests and compare these with data on π^0 and positron showers gathered under high intensity running conditions over periods of several months. We demonstrate the ability of our detector to measure photon directions to ±30 mr rms and time-of-arrival to within ±6 nsec rms.

Our detector was designed to be used at Fermilab primarily to detect 5 to 100 GeV photons from the decays of π^0 and η mesons produced in dissociation processes[3]. Experimental goals dictated the following requirements:

1. Ability to handle rates of 5×10^4 hits per channel per second.
2. Position resolution better than 1.5 mm rms.
3. Energy resolution better than $20\%/\sqrt{E(\mathrm{GeV})}$.
4. Good photon-hadron discrimination.
5. Ability to provide selective triggers.
6. Stable operation.
7. Uniform response over the active area.

The choice of a liquid argon calorimeter was forced by the need to meet these requirements, especially 2, 6 and 7, at low cost.

II. Construction and Cryogenics

Figure 1 shows an exploded view of the detector. It consisted of 61 lead sheets (2 mm thickness) and 62 copper-clad G-10 sheets separated by G-10 spacers along the edges, and by small G-10 pins in the active area. The entire sandwich was held together and attached to its support structure by stainless steel rods. When immersed in liquid argon, the detector was 25 radiation-lengths and 1.2 pion interaction-lengths thick. The liquid argon gaps were 2 mm.

The lead sheets were obtained from St. Joe Mineral Corp., Monaca, Penn. This lead (type SJM620), used in automotive batteries, is rather hard and inflexible compared to antimony lead. The delivered sheets were reasonably uniform in thickness (variations were less than ±50μ), but suffered from severe waviness of the surface. Flattening by re-rolling proved to be impossible because of the hardness of the lead. The required flatness was finally achieved by processing the sheets with a "roller-leveler" at a steel-rolling factory.

After flattening, the sheets were stacked on an aluminum jig plate for machining of the edges and drilling of the 19.8mm diameter beam hole. Next followed degreasing with freon and inspection of the surfaces. Gouges were sanded smooth, and gritty inclusions, apparently pressed into the surface during the initial rolling, were removed. Surface flakes, up to ¼mm thick and 1cm across, were often found loosely attached to the sheets. These were removed and the resulting pitted areas were smoothed.

The copper-clad G-10 sheets were etched to form strips of 1.27 cm in pitch, with 0.5mm interstrip gaps. The strips extended along the X- and Y-directions on alternate sheets. The strips with same X and Y positions along the axis of the detector were connected to a single amplifier channel. However, the Y-measuring sheets were divided electrically into left and right sections, and the LAC read-out was further subdivided into front and back halfs (each containing the same amount of ∿12 radiation lengths of material). A silk-screening step in the etching process was responsible for ±1mm variations in the positioning of the strips from one sheet to the next. This variation exceeded our specification of ±0.5mm, but spatial resolution proved excellent in spite of this. The copper surfaces were left bare. The corrosions that quickly formed were removed and prevented from recurring by bathing the sheets in a mild acid solution followed by a weak NaOH bath and distilled water rinse.

During construction of the assembly, we carefully measured thicknesses along the detector edges so as to compensate for varying spacer thicknesses by inserting 3 mil mylar shims between the spacers. The edge thickness of the finished stack was uniform to within ± 0.5 mm out of a total thickness of 50 cm.

The lead sheets in the stack were free-standing. This was achieved by placing G-10 frames, that were ¼ mm thicker than the nominal lead, around the edges of the lead sheets; the lead was therefore not held tightly when the assembly was compressed at the edges with the stainless steel rods; consequently, the lead sheets were free to contract and expand independently of the rest of the structure, which, being made almost entirely of G-10, had a uniform coefficient of thermal expansion. The beam hole in the lead sheets was placed 1.5 mm higher than in the G-10 sheets so that all holes would be concentric at liquid argon temperature. In order to minimize beam interactions inside the detector, a thin-walled, evacuated quartz tube was inserted in the beam hole.

The detector support consisted of a welded aluminum cradle with 1.3cm thick G-10 underneath and behind the detector. Oversize holes in the G-10, and teflon bushings between aluminum and G-10, allowed for differential contraction. A key on the bottom G-10 sheet provided for accurate alignment of the various layers.

The detector-cradle assembly was suspended from a flat stainless-steel cover plate for the cylindrical cryostat (see Figure 2). This vacuum-insulated vessel was supported in a tall steel structure (tower) which also provided the means to raise and lower the cover plate and suspended detector. The whole tower structure could be moved on air pads so as to sweep the detector horizontally across the beam.

A catwalk, attached to the tower, provided access to the detector when it was out of the cryostat. Access to the cryostat top, even when the full intensity beam was passing through the detector, allowed fast de-bugging and easy maintenance of the amplifier-readout system and trigger electronics, and proved to be more a necessity than merely a convenience.

About 3000 liters of liquid argon sufficed to cover the detector. Welding grade argon was cleansed of its oxygen content (usually less than 4 ppm) by passing the gas over a palladium catalyst along with a small flow of hydrogen. The resulting water vapor traces were removed by passing the gas through room-temperature dessicants that were followed by a molecular sieve, operated at dry ice temperature. Oxygen content at the purifier output was typically a few tenths of a ppm. The purified gas was liquified in a storage dewar from which the liquid could be transferred to the detector cryostat via a vacuum-insulated transfer line. Cryogenic temperatures were maintained in each vessel by sensing the liquid argon vapor pressure and controlling the flow of liquid nitrogen through internal cooling coils. Even after many months of storage, and several transfers between storage dewar and detector cryostat, oxygen content remained at or below the 1 ppm level.

In the detector cryostat, temperature and liquid level were directly monitored by thermistors. If the detector had to be accessed for repairs, the liquid would be transferred out of the cryostat and twelve 100-watt heaters on the detector cradle could be powered to speed warm-up.

The cylindrical shape of the cryostat made it necessary to include a thin-walled box to displace the liquid argon in front of the detector (see Fig. 2). This stainless steel container was packed with hollow glass microspheres (density approximately .08 gm/cc) to prevent it from imploding when it was evacuated.

III. Electronics

Figure 3a shows the block diagram of the front-end electronics for the detector.[4] The ganged strips from the detector, with a total capacitance of 2.5 nF/channel, were connected to individual amplifiers through multiconnector flat cables that had impedances of 10Ω. The cables were back-terminated at the detector. The input impedance of the amplifiers (~ 40 Ω at 0.1-30 MHz) was only approximately matched to that of the cables; consequently, the cables were properly terminated only at one end. This did not cause difficulty (e.g. ringing) because the pulse rise-times were long (~ 300 ns).

The charge-sensitive amplifier consisted of a capacitively fedback amplifier with a high gain-bandwidth (approximately 10^8 Hz). The amplifier output passed through a 400 nsec lumped delay element to the sample-and-hold section. The CMOS switches SW1 and SW2 could be opened at the times appropriate for measuring the rise in the output for the event of interest. In Figure 3b, the second hit is measured by having the switches open at the times shown. After both switches have opened, the output of the difference amplifier is proportional to the integrated charge for the event of interest. This novel method of baseline subtraction obviated the need for complicated and expensive pole-zero cancellation to achieve fast baseline restoration. Another advantage of this method over single switch sample-and-hold designs is that the small noise charges which are injected onto the holding capacitors when the switches open tend to cancel out in the difference amplifier, thereby improving pedestal stability and reducing system noise in the analog outputs.

Outputs for triggering purposes were provided by another difference amplifier driven by the front end. Baseline restoration was accomplished by delay-line differentiation using a 200 nsec tap in the lumped delay element. The fast trigger outputs could be appropriately weighted, summed and discriminated to form an overall calorimeter trigger decision.

When the final event trigger was satisfied, the sample-and-hold switches were opened so as to "trap" the desired event. The sampled signals were then digitized and read as shown in the block diagram in Figure 3c. Twenty amplifier cards and one scanner module were housed in each of six CAMAC crates. The scanner would select one of the amplifier cards and one of the four channels on that card. It would then multiplex into itself the sampled-and-held output of that channel. If the amplifier output exceeded a specified readout threshold, the scanner would send the amplifier analog output to the Master Controller module, along with a "Data Available" signal. This controller module would digitize the amplifier analog output and send the digitized result, along with channel address information, to a CAMAC buffer memory module. After all channels over threshold were digitized, the buffer memory was read by the PDP-15 online data acquisition computer.

A more complete description of the readout electronics may be found elsewhere.[4]

IV. Event Reconstruction

During one experiment (E272), an amplifier channel was read out only if the signal in it was larger than a preset threshold (corresponding typically to 100 MeV deposited per channel). In a later experiment (E629), many soft (1-2 GeV) photons had to be detected, so all channels were read out for each trigger.

The event reconstruction for both experiments used the same program, with only some fitting parameters being different. In the first two steps the two coordinates (X,Y) for the front of the LAC were treated separately. In the first step, groups of neighboring strips containing significant energy were found, and in a second stage these groups were split into individual peaks. Two peaks were considered distinct if at least one channel between them had a lower pulse height than either of the peaks. The projected (X or Y) energy was determined for each peak, after the tails from neighboring peaks had been subtracted. This procedure was iterated until the energies and locations of all peaks in a group were stable in successive iterations. In order to minimize the sensitivity to neighboring peaks when determining the energy in each peak, an algorithm was developed which used the measured shower shape to predict the overall energy and position from only three pulse heights: the peak channel and the two immediately neighboring channels.

After all peaks were identified in the front of the LAC, in both the X and Y views, the two views were correlated using the energy as the correlation parameter. Subsequently, the energies observed in the back of the LAC were added to the larger signals identified in the front, to form the total shower energies. Because of the good intrinsic resolution, and due to the fine interleaving of the X and the Y views, the pulse height in the two views is highly correlated. Figure 4 shows a scatter plot of the pulse heights in the X and Y strips for electrons from Ke_3 decays. The two projections each provide an independent energy measurement which is a factor of $\sqrt{2}$ less accurate than the overall energy obtained from the sum of the two measurements.

The correlation between the two views had to take into account the possibility that two photons overlap each other in one view while being separated in the other. After eliminating all correlated isolated peaks from further consideration, the reconstruction attempted to correlate the energy in two peaks in one view with the energy of a single peak in the other view. When such an overlap of two photons was found, the positions of the two photons in the overlapping view were redetermined by an overall fit to the peak, using the energy information obtained from the non-overlap view. This two parameter (2 positions) fit to overlapping photons converged rapidly even if the peak was not completely separated from the tails of other nearby peaks, while a 4-parameter fit (2 positions and 2 energies) even to a peak with an obvious shoulder tended to yield poor convergence and ambiguous results.

V. Detector Performance

A. Description of the experiments

The detector was used in two Fermilab experiments, E272 and E629, between 1978 and 1981. The goal of E272 was the measurement of coherent dissociation processes, primarily coulombic production in nuclei.[3] E629 was a test of the feasibility of measuring direct photon production at high p_T using a liquid argon calorimeter (LAC). In both experiments the detector performed reliably and provided excellent resolutions. In this section we present these results and compare resolutions achieved under various running conditions.

Figure 5 shows a plan view of the E272 layout. Charged particles from interactions in the target and from $K^+ \to \pi^+ \pi^0$ and $K^+ \to \pi^0 e^+ \nu$ decays of beam kaons were momentum-analyzed with four stations of drift chambers and an analyzing magnet. Photons passing through the magnet aperture were detected in the LAC, which was centered on the (deflected) beam. (The beam was focussed so as to pass through the 1.8 cm central beam hole of the LAC.) Incident beam energies were 156, 200 and 260 GeV. The beam intensity was typically 5×10^5 particles per second onto a .03 interaction length target. Most of the data were accumulated with a 200 GeV positively charged beam; it is this set of data that we will concentrate on here.

At various times during E272, we retuned the beam energy to 50 GeV, at which energy electrons constituted about 10% of the negatively charged beam. The detector was moved in small steps across the beam so that each X-measuring strip was hit by about 500 electrons. A vertically-deflecting dipole magnet upstream of the target was used to sweep the beam across the Y-measuring strips on each side of the detector. Because the energies of the electrons were smeared by bremsstrahlung in material in the beam line upstream of our apparatus, the momentum of each electron was determined from data using the charged-particle spectrometer.

These sweeps constituted the electron calibration of the detector. The data were used to find the relative gains of individual amplifier channels. Calibration constants in the reconstruction programs were adjusted to give the best agreement between the electron energies and positions given by the LAC and those measured by the charged-particle spectrometer. For both energy and position, the spectrometer provided more accurate measurements than the LAC; thus the observed resolutions are primarily due to the LAC.

During E272 data-taking, $K^+ \to \pi^+\pi^0$ and $K^+ \to \pi^0 e^+ \nu$ decays of beam kaons were recorded along with events from the primary triggers. Positrons from the Ke_3 events provided a natural means for studying the linearity of the detector,and a way of comparing energy and positions resolutions achieved under data-taking conditions with those obtained during the special electron calibration studies. $K^+ \to \pi^+\pi^0$ events were used to study the system's ability to handle two showers which are near each other and thus overlap to varying degrees in one view, or in both.

Figure 6 shows the experimental setup for E629. The detector was centered at about 110 mr relative to the beam line, with the beam tuned for 200 GeV positively charged particles. The intensity was typically 10^7 particles per second. In this experiment we measured the production of π^0 mesons and single (direct) photons produced in the p_T range from 2.5 to 5 GeV/c. The corresponding energy range was approximately 25 to 50 GeV. Nine planes of proportional wire chambers tracked particles on the LAC side, but there was no momentum analysis. Due to severely restricted beam time at Fermilab in 1981, there was not sufficient time for an electron calibration during the execution of E629. Instead, we measured relative amplifier gains by injecting pulses of fixed charge into the amplifiers. The E629 data will demonstrate that the LAC system can handle high particle-multiplicities, determine the direction of incidence of photons, and provide excellent timing information.

B. Charge Collection

In Figure 7 we show the ratio of the collected charge to that available as a function of applied voltage, where the total available charge is given by

$$Q = ef \frac{E(\mathrm{GeV})}{52.8 \times 10^{-9}} \qquad (1)$$

where e is the electron charge, E is the incident photon (or electron) energy, and f is the fraction of the photon energy deposited in the liquid argon. For our detector f was 0.16. At our operating voltages the detector collected about 41% of the total charge given by equation (1).

In a report on a liquid argon detector used at the ISR, Cobb, et.al.[2] state that the collected charge in Eq. (1) is correct for muons, but ∿30% too high for incident electrons. The data in Figure 7 do not seem to approach even this lower level. For reasons not well understood, the charge collection improved by 30% during the execution of E272. As inferred from the observed value of the reconstructed ^{0} mass and of the total energy from $K2\pi$ events, this produced a small increase in pulse height as a function of time. We have verified that the applied voltage and the amplifier/ADC gains were constant and are therefore compelled to attribute this gain increase to a slowly improving charge collection. We suspect that the improvement may have been due to the slow freezing out of unknown electronegative impurities in the liquid. The final value for charge collection was about 55% of that given by equation (1), which is in fair agreement with the expectations of Cobb, et.al. The E629 charge collection remained constant at the indicated operating point. For both experiments, the observed loss in charge is not attributable to the presence of oxygen.

The variation of gain with time illustrates a virtue of the liquid argon calorimeter. We found it easy to monitor this slow change, and thereby correct the reconstruction programs simply by multiplying the gain constants of all channels by a single, time-dependent, factor.

C. Electron calibration

In Figure 8 we present the energy and position resolution for the 50 GeV electron calibration in E272. Figure 8a shows the distribution in the variable E_{LAC}/E_{SP} , where E_{LAC} and E_{SP} are the electron energies as reconstructed by the photon detector and spectrometer respectively. The contribution of the spectrometer resolution to the observed width is given by the narrow peak, and is clearly negligible. The curve through the data is a gaussian whose rms width is $\Delta E/E = 1.46\%$. Expressed in customary terms, $\sigma(E)/E = 10.3\%/\sqrt{E(\mathrm{GeV})}$, for the 50 GeV electron calibration.

Figure 8b shows the position resolution. Again, the narrow gaussian shows the contribution to spatial resolution expected from the spectrometer. The gaussian curve through the data points has an rms width of 0.67mm . Unfolding the spectrometer resolution, we arrive at a spatial resolution (in one projected view) of 0.58 ± 0.07 mm for the LAC.

These excellent resolutions have been achieved under the following conditions:

1. The beam intensity was low.
2. Only one particle was incident on the LAC per event.
3. The data were taken over a short period of time; thus the effect of slow drifts in pedestals and gains was minimal.
4. The reconstruction program calibration constants were tuned to achieve the best results.

In the following section we compare these results with resolutions obtained under normal experimental conditions.

D. Performance during E272

Figure 9 shows the energy resolution for positrons from Ke_3 decays collected during E272 data-taking. The plotted points are the squares of the rms widths for the distributions obtained from a comparison of E_{LAC} and E_{SP}. That is,

$$\sigma_E^{\ 2} = \left((E_{LAC} - E_{SP})_{rms}\right)^2 \qquad (1).$$

The dashed line through the data is given by

$$\sigma^2(\mathrm{GeV}) = \left(0.14\,\sqrt{E(\mathrm{GeV})}\right)^2 + (0.55)^2 \qquad (2).$$

The result for the electron calibration is shown for comparison. Resolution for these data is worse than for the 50 GeV calibration point by a factor of ∿1.5.

We attribute this difference to the following effects:

1. High beam intensities will occasionally produce amplifier pedestal shifts due to particles, uncorrelated with the Ke3 event, striking the detector at random times.
2. For Ke3 events, the photons from the π^0-decay will sometimes strike the LAC near the position of the positron, this will produce overlapping showers that lead to inaccuracies in reconstruction of the positron energies.
3. The Ke3 data were accumulated over several months, whereas the calibration data were gathered in about 18 hours. Consequently, the calibration data do not suffer from inaccuracies in monitoring drifts in pedestals and gains of individual amplifier channels.
4. The positrons from Ke3 events are spread over the face of the LAC in X and Y, whereas, for the calibration data, the electrons (in the X-sweep) always hit the detector at the same Y-position. From studies not presented in this paper, we infer that the charge collected by any typical X-measuring strip varies with the Y-position of the hit along that strip. This variation is somewhat greater than 1%; it will be reflected in the Ke3 resolutions but not in the calibration data.

Next we present π^0-mass resolutions from $K^+ \to \pi^+ \pi^0$ decays. For various π^0-energy intervals between 40 and 180 GeV, we have calculated the rms widths of the $\gamma\gamma$ spectra at the π^0 mass. The data are shown in Figure 10. For simplicity, we have used only events for which the ratio of the two photon energies falls in the range 0.5 to 2.0; that is, we have excluded events with highly asymmetric π^0 decays. The dashed curve is the result of a calculation using the energy and position resolutions obtained from the Ke_3 events. The calculation agrees with the data points to within 50% between 120 and 160 GeV, but is a factor of two low at the extreme energies. Thus, the observed mass resolution does not appear to be dominated by the resolutions for the individual photons, but rather by difficulties in reconstructing events with two nearby, and often overlapping, showers. The smooth curve in Figure 10 demonstrates this. It is from a Monte

Carlo calculation in which photons from simulated $K^+ \rightarrow \pi^+ \pi^0$ events deposited energy in the detector according to the measured shower shape. The energy in each strip was then given an rms jitter of $\sigma = 0.14 \sqrt{E_{strip}(\mathrm{GeV})}$. The resulting pulse height array was passed through the reconstruction program, and used to calculate π^0 mass resolutions for the reconstructed events. The Monte Carlo agrees with the observed resolutions much better than does the curve calculated from the single shower resolutions obtained from Ke_3 events.

E. Performance during E629

The E629 data is characterized by higher multiplicities than those in E272. Figure 11 demonstrates the ability of our LAC to permit reconstruction of these complicated events. The 2γ mass distributions (for p_T greater than 2.5 GeV/c) in the π^0 and η regions are presented for events with 2, 3, 4 and ≥ 5 photon showers in the detector. The mass of each 2γ combination is plotted; for the 4 photon distributions, for example, up to six combinations can be plotted for each event. A clear π^0 signal is evident for all multiplicities, and the π^0 mass resolution does not deteriorate dramatically as multiplicity increases. An $\eta \rightarrow \gamma\gamma$ signal of constant width is evident for all but the highest multiplicities.

The major backgrounds for high p_T direct-photon measurements can be categorized as follows. (1) Single photons or hadrons that originate upstream of the target (typically, parallel to the beam line), in random coincidence with a beam interaction in the target; (2) Triggers in which two beam interactions occur within a short time span of each other, thereby causing energy pile-up and distortion of signals from the LAC; (3) Events that have only one of the photons from π^0 or η^0 decays hitting the LAC. The third kind of background can be handled in a straightforward manner using the measured π^0 and η^0 yields. To combat the more severe backgrounds from items (1) and (2), we used the front and back section of the calorimeter to determine the directions of the incident photons, and we timed each amplifier's fast output pulse with time to digital converters (TDC's).

Figure 12 demonstrates the method used for eliminating photons that did not originate in the target. A photon from the target, traveling along the dashed line, will deposit most of its energy in the front half of the detector at position X_F, and the rest in the back half, at position X_B. On the other hand, a photon or particle striking X_F, while traveling parallel to the beam direction will have its energy displaced from the expected position in the back by $X_B^{'}-X_B \equiv \Delta X_B$. For photons that originate from the target the ΔX_B distribution should be centered at zero. Figure 13 is a scatter plot of ΔX_B versus X_F for events in which only one photon was found in the detector. Two distinct bands are present: one, corresponding to sources from the target, centered at $\Delta X_B = 0$ (independent of X_F), and another tilted relative to $\Delta X_B = 0$. The tilted band is that expected for the dependence of ΔX_B on X_F for off-axis photons traveling parallel to the beam direction. (The two horizontal gaps are due to dead amplifiers in several of the back X-strips.) Taking the rms width of the central peak, and estimating the effective lever arm between front and back of the LAC, we find an angular resolution for determining the directions of incident photons of ±30 mr (rms).

As mentioned previously, the amplifiers for all fron X strips were connected to low-threshold discriminators whose outputs went to time digitizers. Figure 14 shows the time of arrival for single photon events in three ranges of p_T. The times were obtained from the TDC channels corresponding to the central X-strips of the photon showers. (The effect of applying a cut in ΔX_B so as to eliminate off-axis photons is shown by the shaded distribution.) In the 2 to 3 GeV/c p_T range, the distribution is a narrow peak centered at the value expected for in-time photons. The rms width is about 6 nsec. In the 3 to 4 GeV/c p_T range, in-time photons from the target still dominate, but for p_T values higher than 4 GeV/c most events are out of time and do not originate from the target. The distribution in Figure 14c can be understood as follows. The veto circuitry protected the trigger against accidentals occurring within 100 nsec before and 50 nsec after a beam interaction in the target. (By accidental, we mean energy deposition in the detector sufficient to satisfy the p_T threshold, but in random coincidence with a low-p_T interaction in the target.) We could not extend the veto protection beyond 50 nsec after the prompt time because of the necessity of gating the LAC amplifiers at the correct interaction time. Before the directionality cut is applied, most of the events in Figure 14c fall beyond this 50 nsec protection cut-off. (As a further indication of the timing resolution, the 19 nsec r.f. structure of the beam spill stands out clearly.) When off-angle photons are removed (shaded data), the resulting distribution shows a small peak of in-time photons, in addition to other small peaks at subsequent r.f. "bucket" times. After cutting away these out-of-time events, we are left with a clean sample of single photons originating in the target and in coincidence with a beam interaction.

To confirm the presence of a direct-photon signal in the E629 data, we had to impose restrictions based on the above described timing and directionality characteristics of the photon showers. In addition, we applied cuts based on the difference in response of the LAC to hadron-induced and to electromagnetic showers.

The use of Pb plates in our LAC provided a device that had a thickness of 25 radiation lengths, but only 1.2 absorption lengths. This allowed a very high level of discrimination between electromagnetic and hadron-induced showers. To be explicit, in Fig. 15a we display the fraction of pions which deposit more than a given percentage of their total energy in the LAC (these data are taken from E272). In Fig. 15b, we present the fractions of pions and electrons (equivalent to photons) which deposit less than a given percentage of their total deposited energy in the back half of the LAC (we have excluded the 30% of the pions that deposit less than 10% of their total energy). It should be noted that a cut on E_{BACK}/E_{LAC} of <.2 will have the effect of eliminating 90% of any pion-induced showers (mislabeled as electromagnetic), at a cost of only 10% of the electrons. When considered in combination with the consequences of Fig. 15a, it is clear that the LAC provides excellent discrimination against hadron background to high-energy photons. Additional discrimination is available in the difference in the transverse shapes of the two kinds of showers. This is demonstrated in Fig. 15c, where we display the shapes observed in E272 for electromagnetic and hadronic data. The results of Fig. 15 for electrons agree entirely with EGS Monte Carlo simulations.[5]

A typical cut of 0.3 on E_{BACK}/E_{LAC} was used to reduce hadron contamination of the photon data. There was no need to apply additional restrictions based on Fig. 15.

VI. Summary

We have described the performance of a large liquid argon photon calorimeter in two experiments at Fermilab. We have presented the first systematic comparison of resolutions achieved in calibration studies with those obtained during normal experimental conditions. The ability of the detector to determine incident directions was clearly demonstrated, as was, for the first time, the use of time digitizers to enhance the rate capabilities of liquid argon calorimeters.

Comparing electron calibration resolutions with high intensity results, we have found similar spatial resolution, but poorer energy determination for the high intensity data. The difference is attributed to reconstruction problems caused by the presence of other photons and particles, and by inaccuracies in long term monitoring of drifts, and to slight (about 1%) variation in detector gain over the active area. The observed π^0 mass resolution cannot be understood solely from the resolutions obtained with isolated showers. Reconstruction inaccuracies caused by errors in unfolding the two nearby photon showers are found to be a dominant source of errors in mass determinations.

We regard the resolutions obtained by our detector as excellent. After the initial setup period, the LAC system performed reliably and required little attention. The liquid argon remained pure over long periods, even when loss of cooling caused venting of the gas through relief valves for periods of up to 12 hours.

Acknowledgments

We thank T. Haelen and his technical staff at Rochester, C. Lindenmeyer and his design group at Fermilab and P. Czarapata, A. Glowacki, C. McGuire, R. Worland and the rest of the crew at Meson for their assistance in the design and execution of our experiments.

References

1. W. J. Willis and V. Radeka, Nucl. Instr. and Meth. 120, 221 (1974).
2. C. Fabjan et al., Nucl. Instr. and Meth. 141, 61 (1977); J. H. Cobb et al., Nucl. Inst. and Meth. 158, 93 (1979); D. Hitlin et al., Nucl. Instr. and Meth. 137, 225 (1976); G. Knies and D. Neuffer, Nucl. Instr. and Meth. 120, 1 (1974).
3. D. Berg et al., Phys. Rev. Lett. 44, 706 (1980); Phys. Lett. B98, 119 (1981).
4. T. F.Droege, F. Lobkowicz and Y. Fukushima, Fermilab Report TM-746 2500.000 (Oct. 1977).
5. R. L. Ford and W. R. Nelson SLAC-210 (June 1978).

Figure Captions

1. Exploded view of the liquid-argon detector.
2. Schematic of the cryostat and cover plate.
3. Block diagram of the front-end electronics and read-out system.
4. Scatter plot of the pulse heights in the X and Y strips of the LAC.
5. Schematic diagram of spectrometer for experiment E272.
6. Experimental arrangement for E629.
7. Ratio of collected to available charge as a function of applied voltage on the LAC.
8. Energy and position resolution for 50 GeV electron-calibration run in E272.
9. Energy resolution for positrons from K_{e3} decays in E272.
10. Mass resolution for π^0's from $K^+ \rightarrow \pi^+\pi^0$ decays, for data from E272, as a function of π^0 energy.
11. Two-photon mass distributions in the π^0 and η mass regions in E629, for 2-γ, 3-γ, 4-γ and >4-γ events, for $p_T > 2.5$ GeV/c.
12. Geometry used for establishing whether photons originate from the target.
13. Scatter plot of the difference between observed and expected positions of showers in the back of the LAC and the lateral position of the shower in the front of the LAC (relative to the center of the detector).
14. Times of arrival of energies for single photons in the LAC as a function of p_T. Photons in-time with interactions in the target are at t=0.
15. Characteristics of showers. (a) The fraction of hadrons that deposit more than a certain percentage of their energy (E_{HAD}) in the LAC.

    (b) Ratio of the energy deposited in the back of the LAC (E_{BACK}) to the total energy (E_{LAC}) observed in the detector. Data are shown for electrons and for hadrons that deposit a measurable amount of energy. (c) The fraction of energy deposited by electrons and hadrons in a 1.27 cm wide strip as a function of the distance of that strip from the centroid of the shower. The electron data are mainly from the 50 GeV calibration run and some from K_{e3} decays (electron momenta between ~ 20 and ~ 100 GeV/c). The hadrons are pions from $K_{\pi 2}$ and $K_{\pi 3}$ decays (momenta between ~20 and 180 GeV/c).

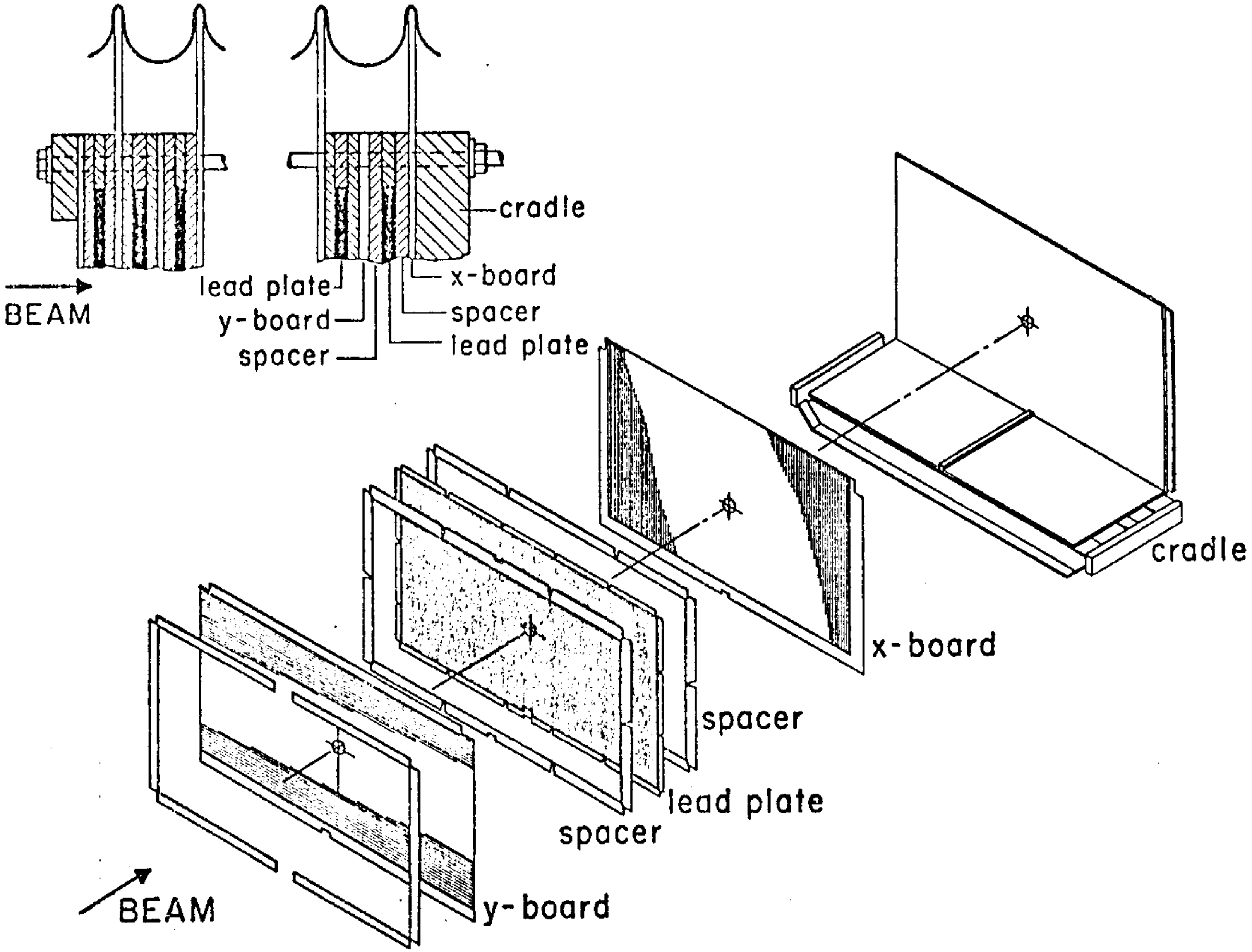
cradle
lead plate
x-board
y-board
spacer
spacer
lead plate
BEAM
cradle
x-board
spacer
lead plate
spacer
y-board
BEAM

Fig. 1

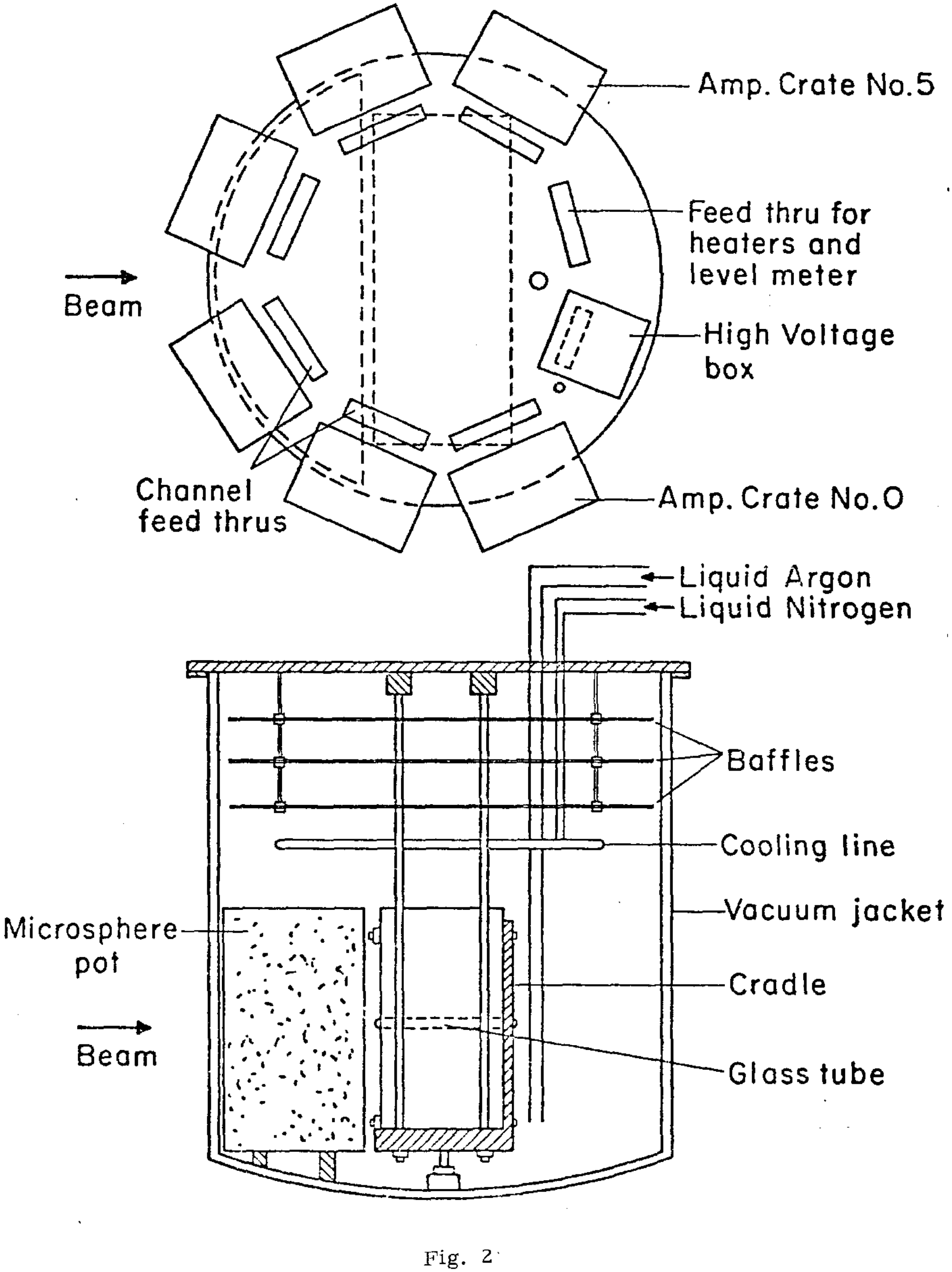
Amp. Crate No.5
Feed thru for heaters and level meter
Beam
High Voltage box
Channel feed thrus
Amp. Crate No.0
Liquid Argon
Liquid Nitrogen
Baffles
Cooling line
Vacuum jacket
Microsphere pot
Cradle
Beam
Glass tube

Fig. 2

a) Electronics for one channel of LAC

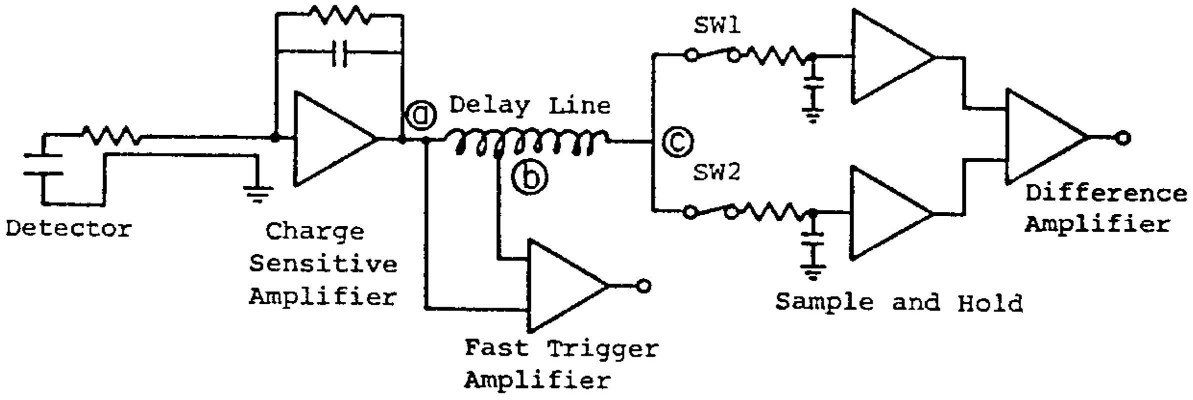

b) Signal at point ©

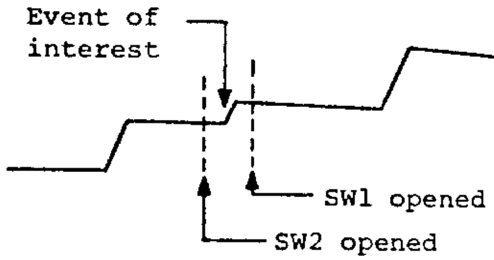

c) Read-out system

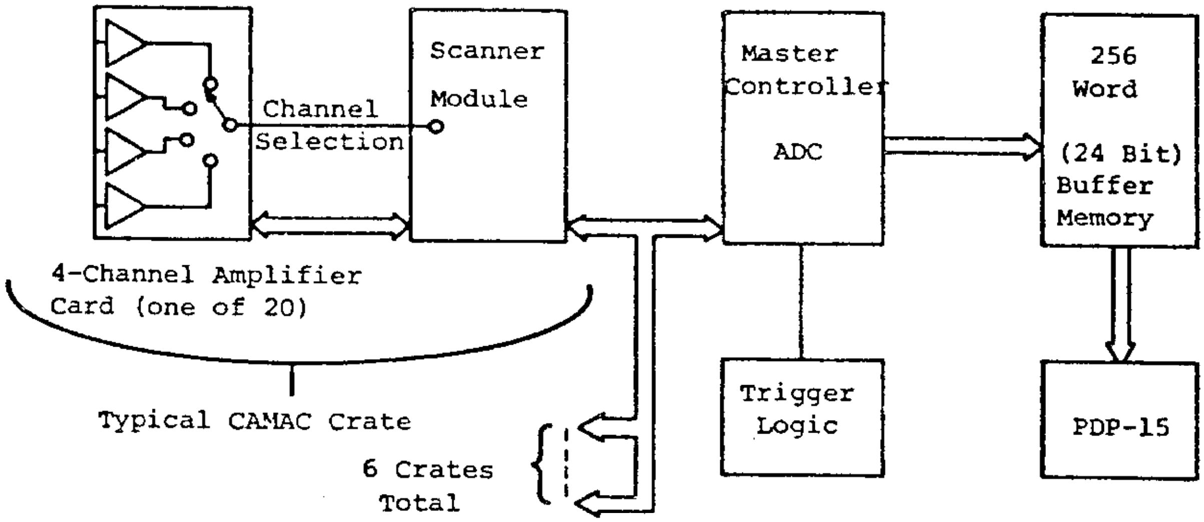

Fig. 3

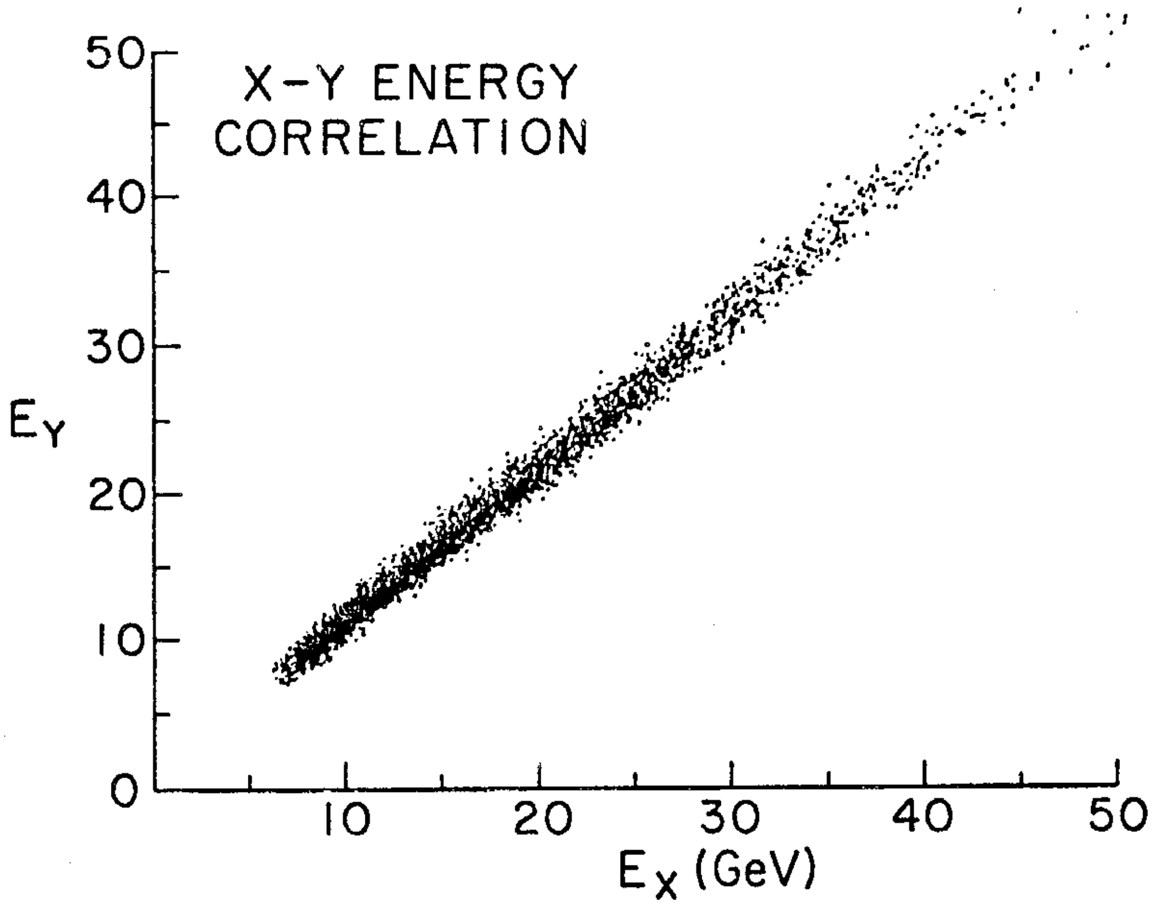

Fig. 4

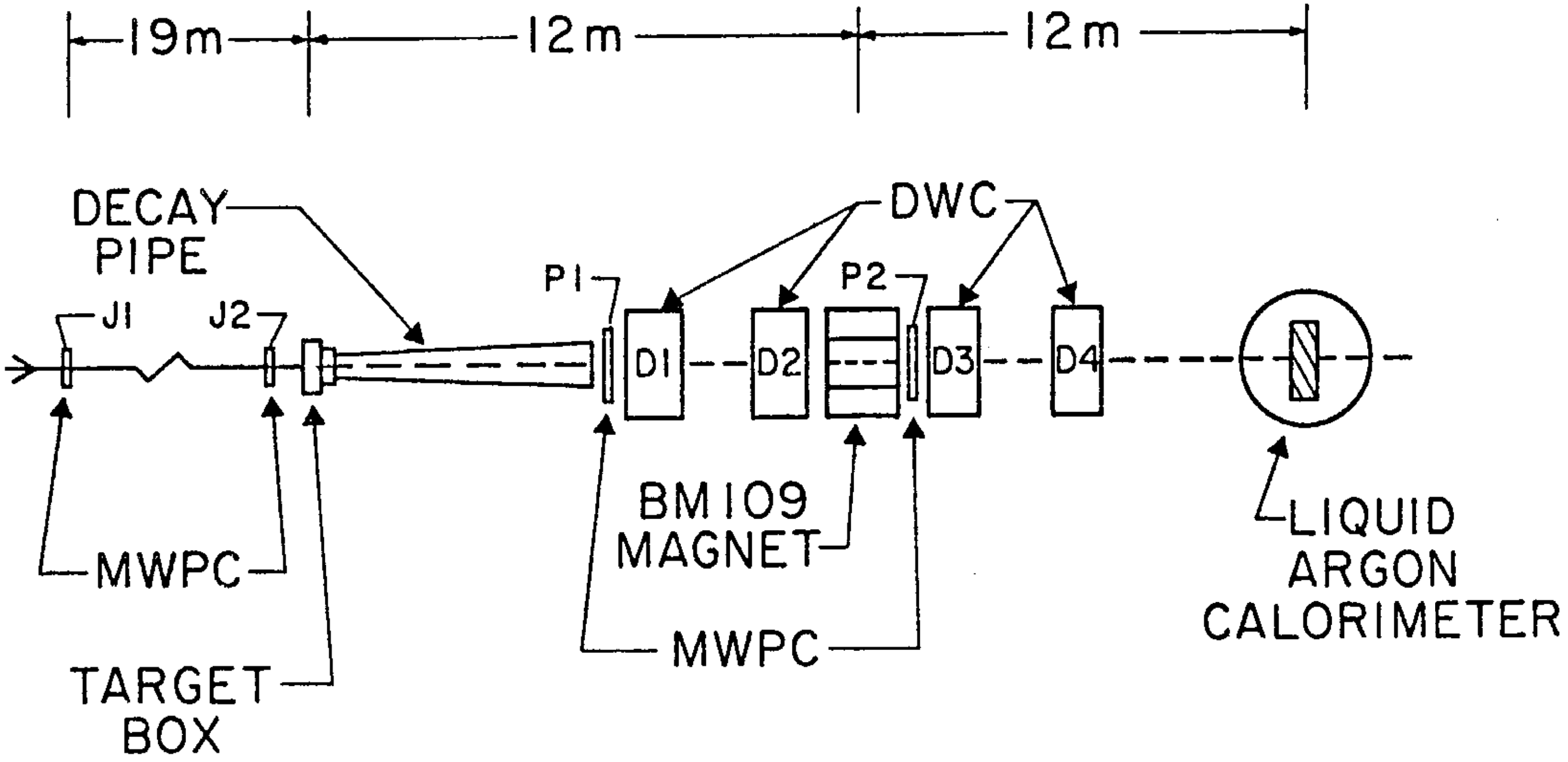
19m
12m
12m
DECAY PIPE
J1
J2
MWPC
TARGET BOX
P1
D1
D2
P2
D3
D4
DWC
BM109 MAGNET
MWPC
LIQUID ARGON CALORIMETER

Fig. 5

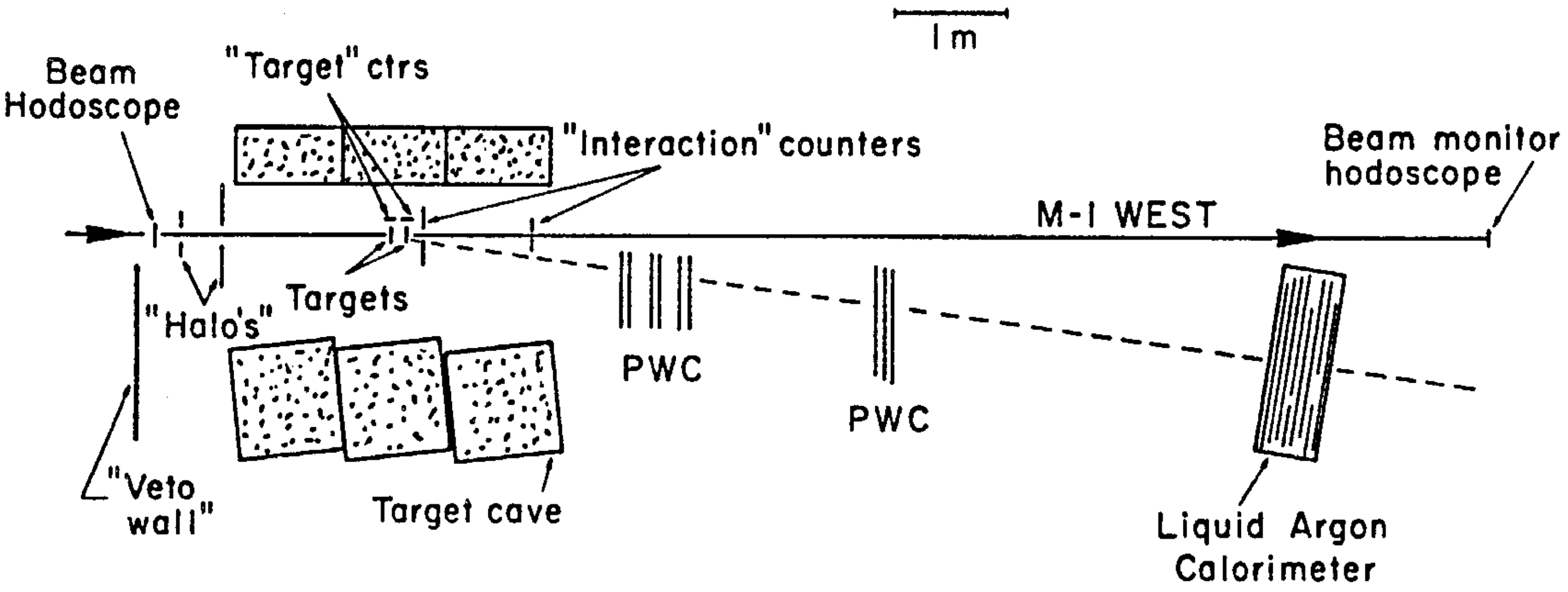
1 m
Beam
Hodoscope
"Target" ctrs
"Interaction" counters
Beam monitor
hodoscope
M-1 WEST
Targets
"Halo's"
PWC
PWC
"Veto
wall"
Target cave
Liquid Argon
Calorimeter

Fig. 6

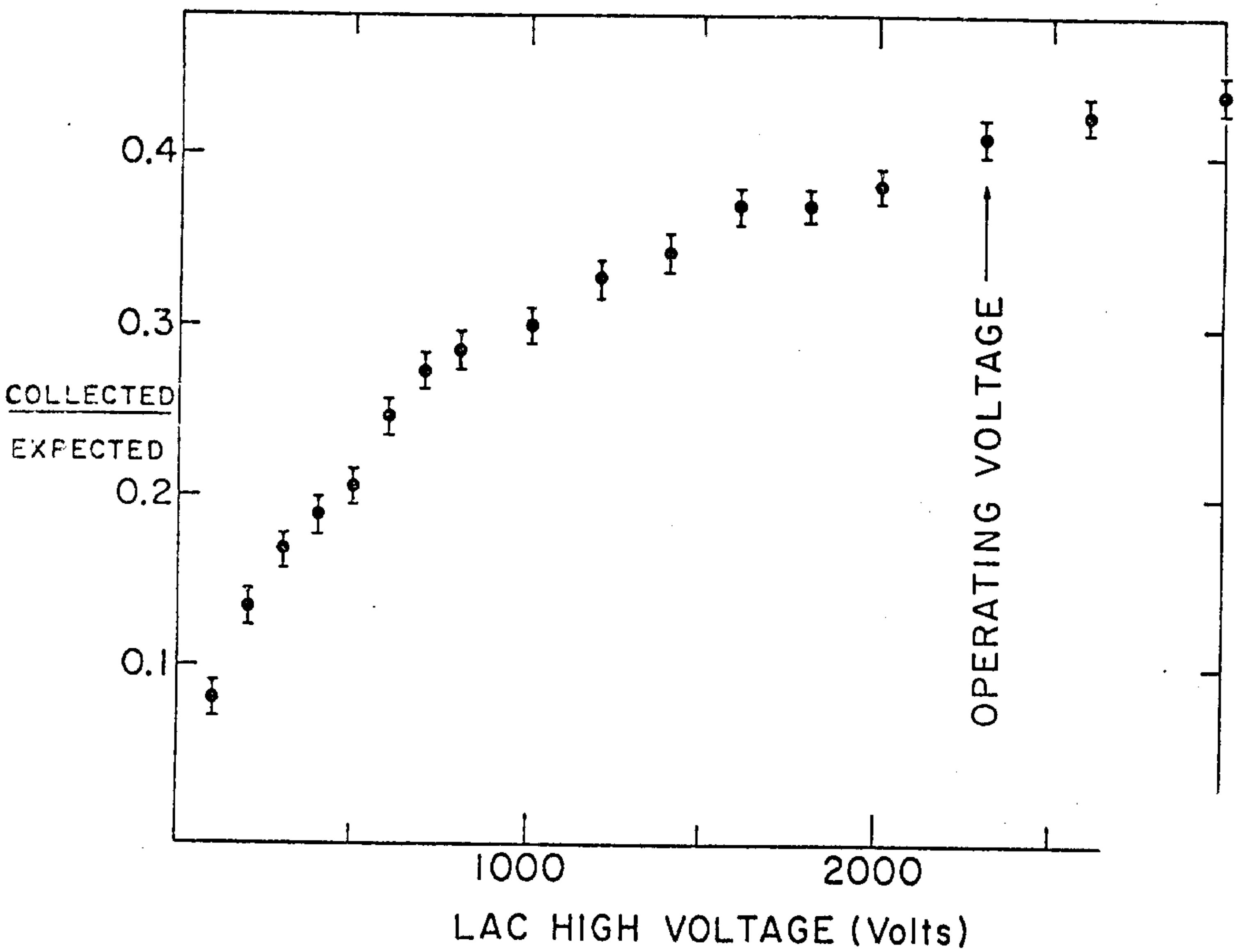
0.4
0.3
0.2
0.1
COLLECTED
EXPECTED
1000
2000
LAC HIGH VOLTAGE (Volts)
OPERATING VOLTAGE

Fig. 7

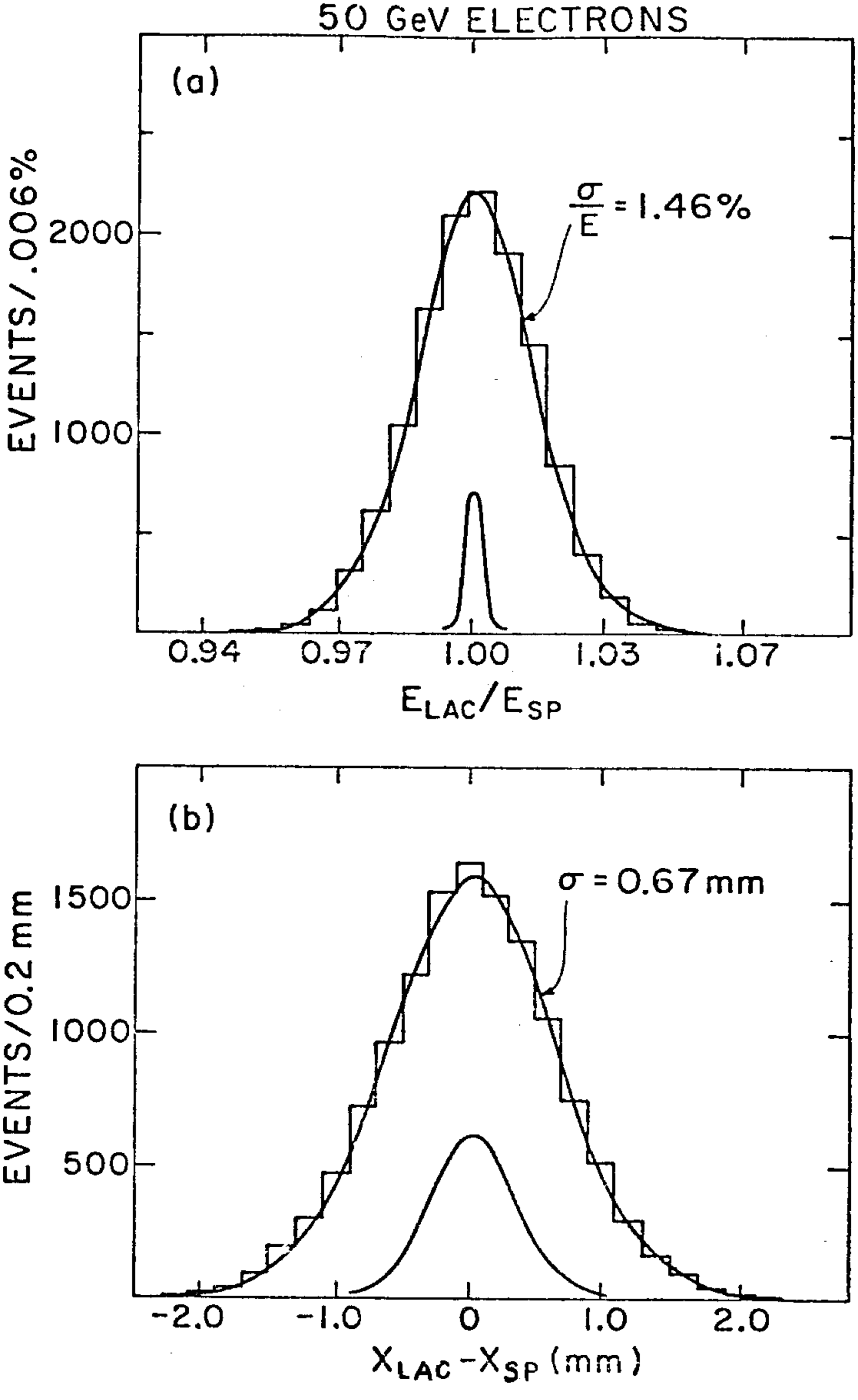

50 GeV ELECTRONS
(a)
EVENTS/.006%
2000
1000
$\frac{\sigma}{E} = 1.46\%$
0.94
0.97
1.00
1.03
1.07
E_{LAC}/E_{SP}
(b)
EVENTS/0.2 mm
1500
1000
500
$\sigma = 0.67$ mm
-2.0
-1.0
0
1.0
2.0
$X_{LAC} - X_{SP}$ (mm)

Fig. 8

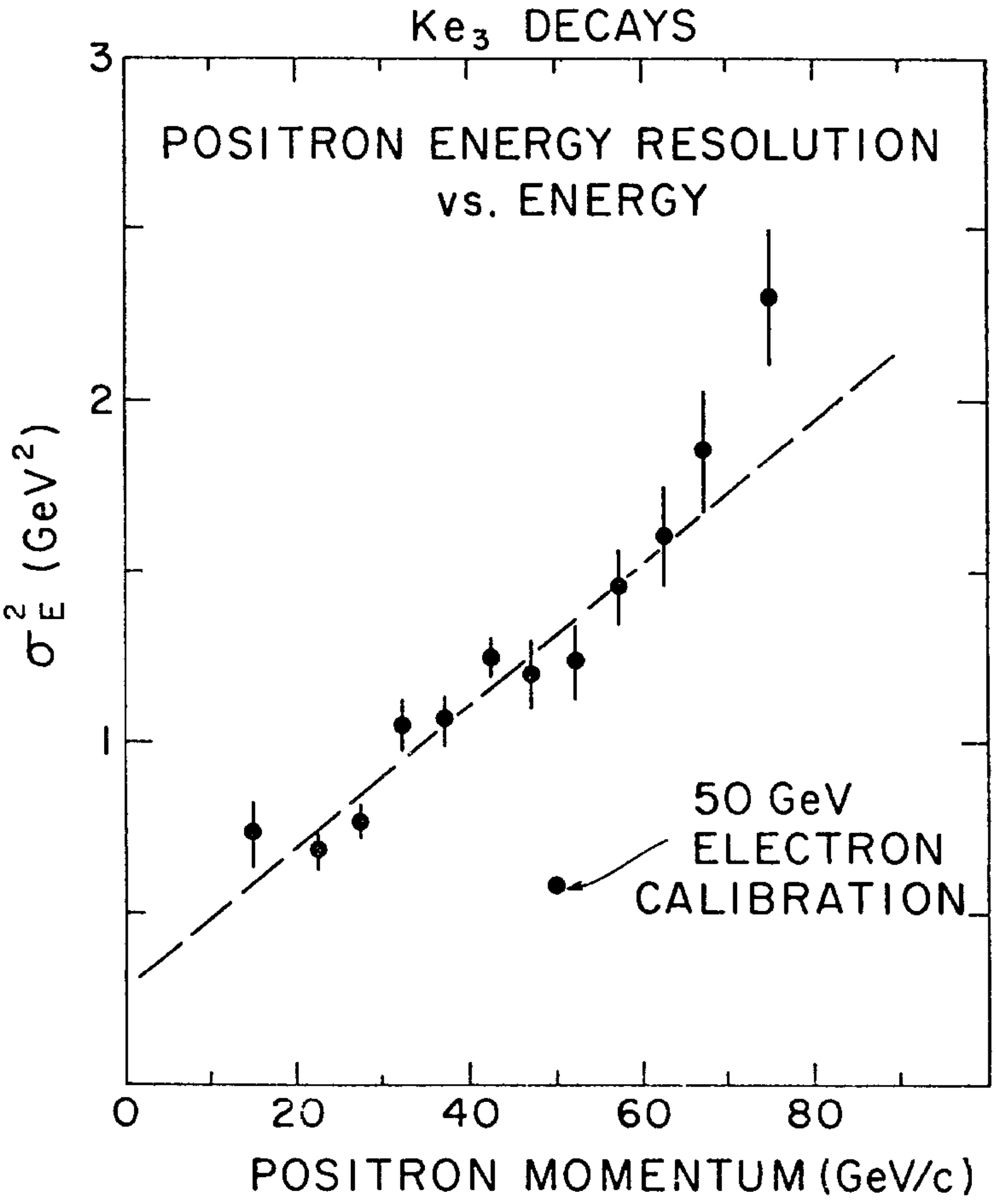
Ke$_3$ DECAYS
POSITRON ENERGY RESOLUTION vs. ENERGY
50 GeV ELECTRON CALIBRATION
σ_E^2 (GeV^2)
POSITRON MOMENTUM (GeV/c)
0
20
40
60
80
1
2
3

Fig. 9

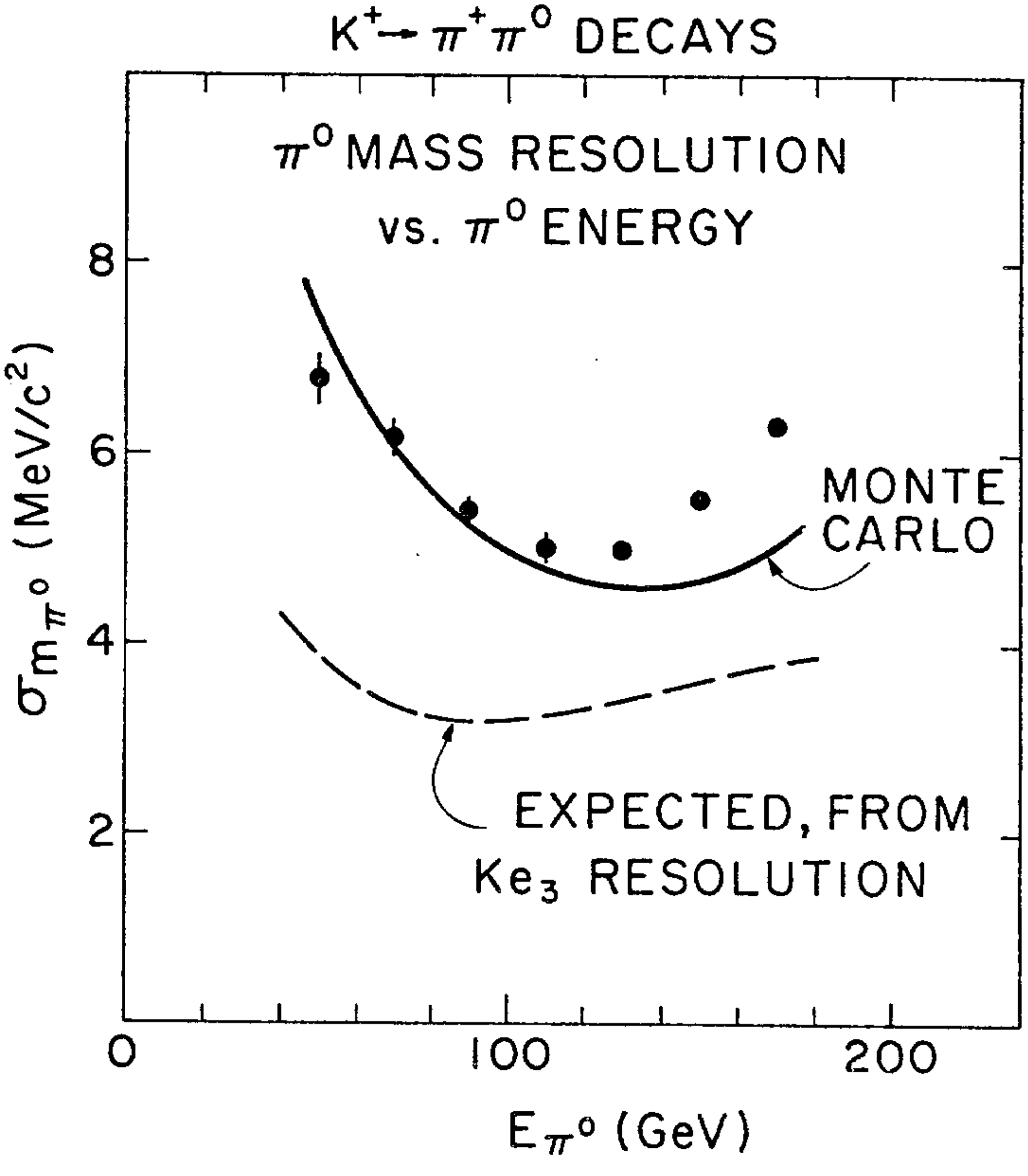

$K^+ \rightarrow \pi^+\pi^0$ DECAYS
π^0 MASS RESOLUTION
vs. π^0 ENERGY
$\sigma_{m_{\pi^0}}$ (MeV/c^2)
8
6
4
2
0
100
200
E_{π^0} (GeV)
MONTE CARLO
EXPECTED, FROM
Ke_3 RESOLUTION

Fig. 10

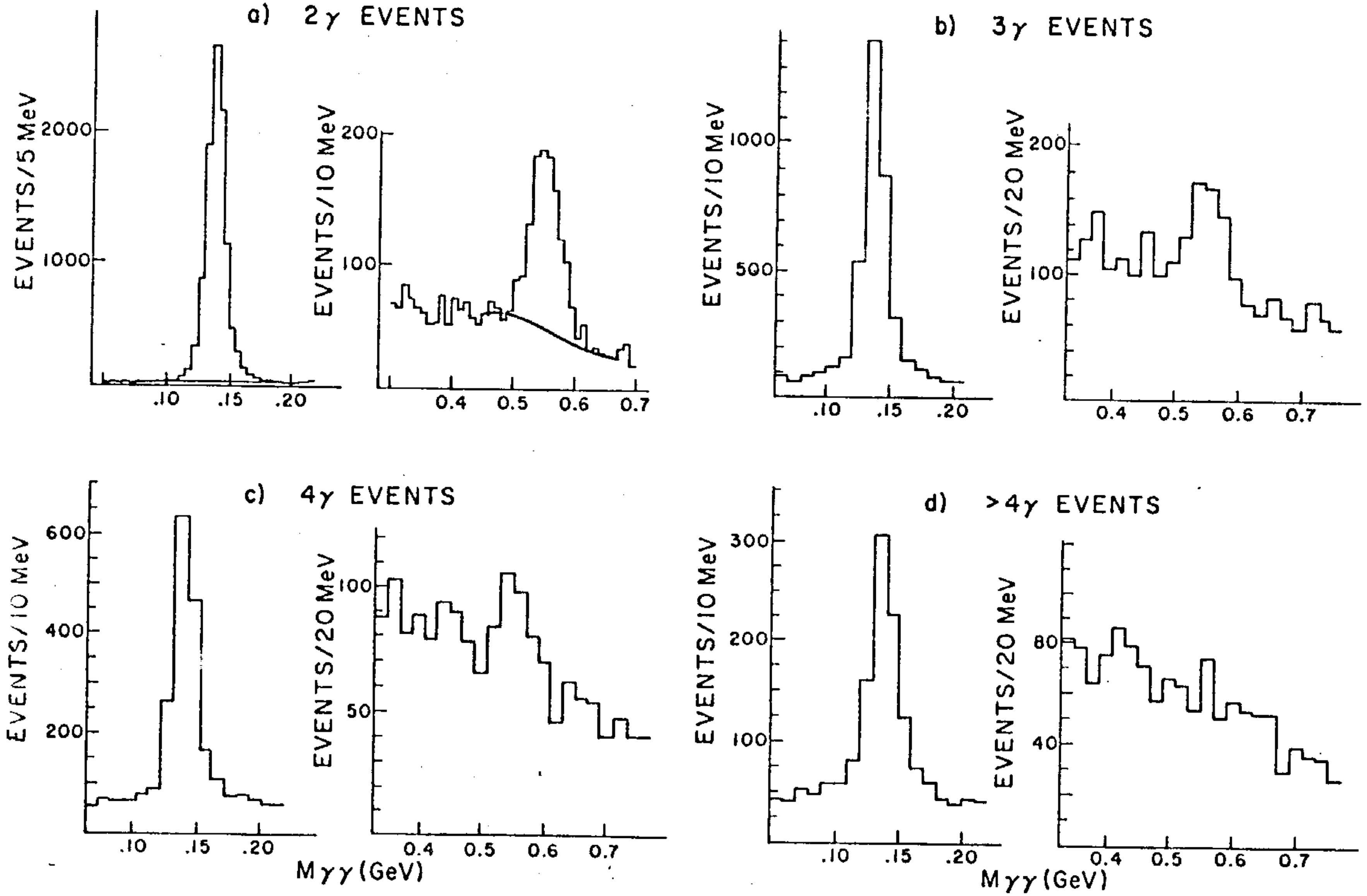
a) 2γ EVENTS
EVENTS/5 MeV
2000
1000
.10
.15
.20
EVENTS/10 MeV
200
100
0.4
0.5
0.6
0.7
b) 3γ EVENTS
EVENTS/10 MeV
1000
500
.10
.15
.20
EVENTS/20 MeV
200
100
0.4
0.5
0.6
0.7
c) 4γ EVENTS
EVENTS/10 MeV
600
400
200
.10
.15
.20
EVENTS/20 MeV
100
50
0.4
0.5
0.6
0.7
Mγγ (GeV)
d) >4γ EVENTS
EVENTS/10 MeV
300
200
100
.10
.15
.20
EVENTS/20 MeV
80
40
0.4
0.5
0.6
0.7
Mγγ (GeV)

Fig. 11

$$\Delta X_B = \frac{T_{LAC}}{D_{LAC}} (X_F - X_O)$$

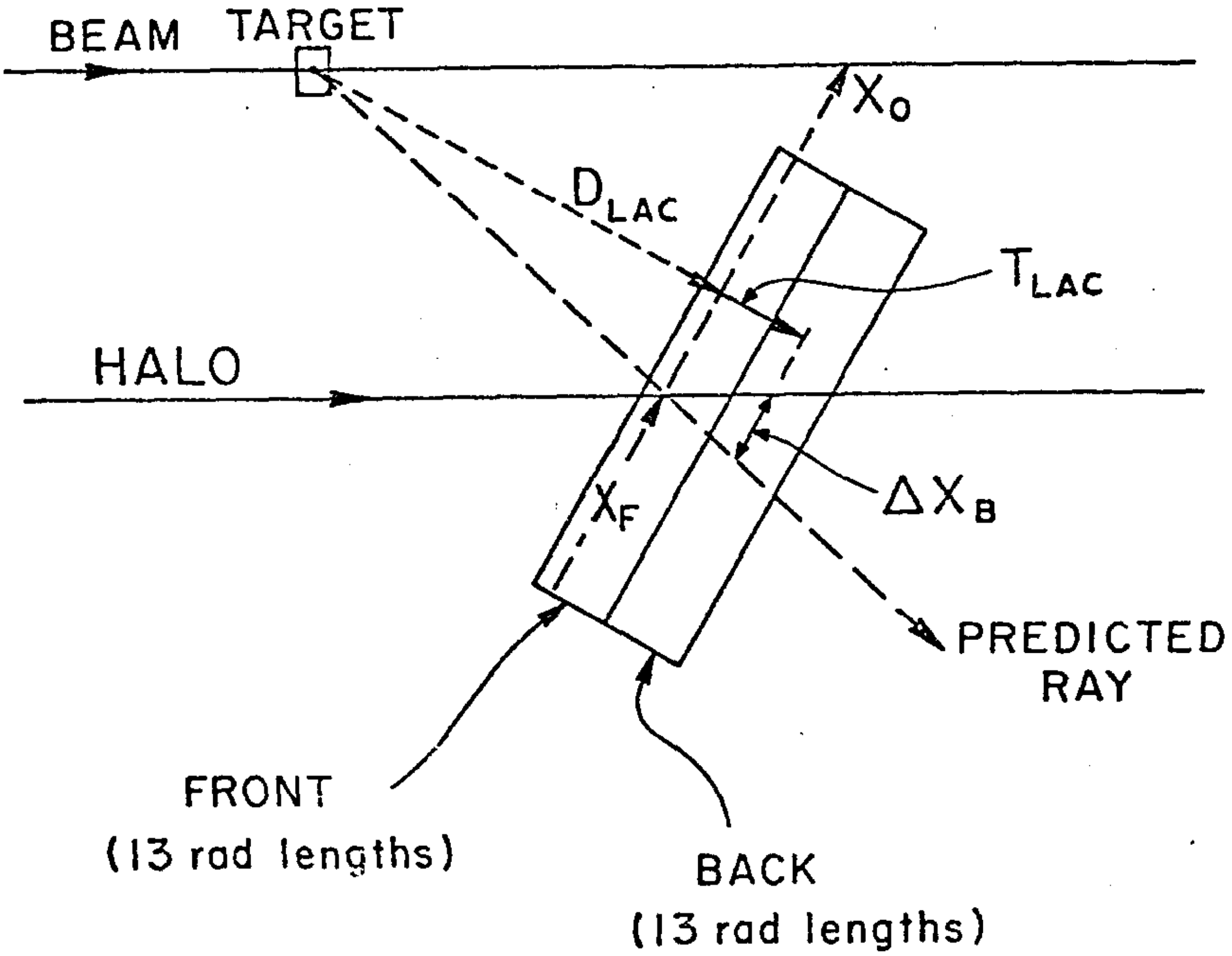

Fig. 12

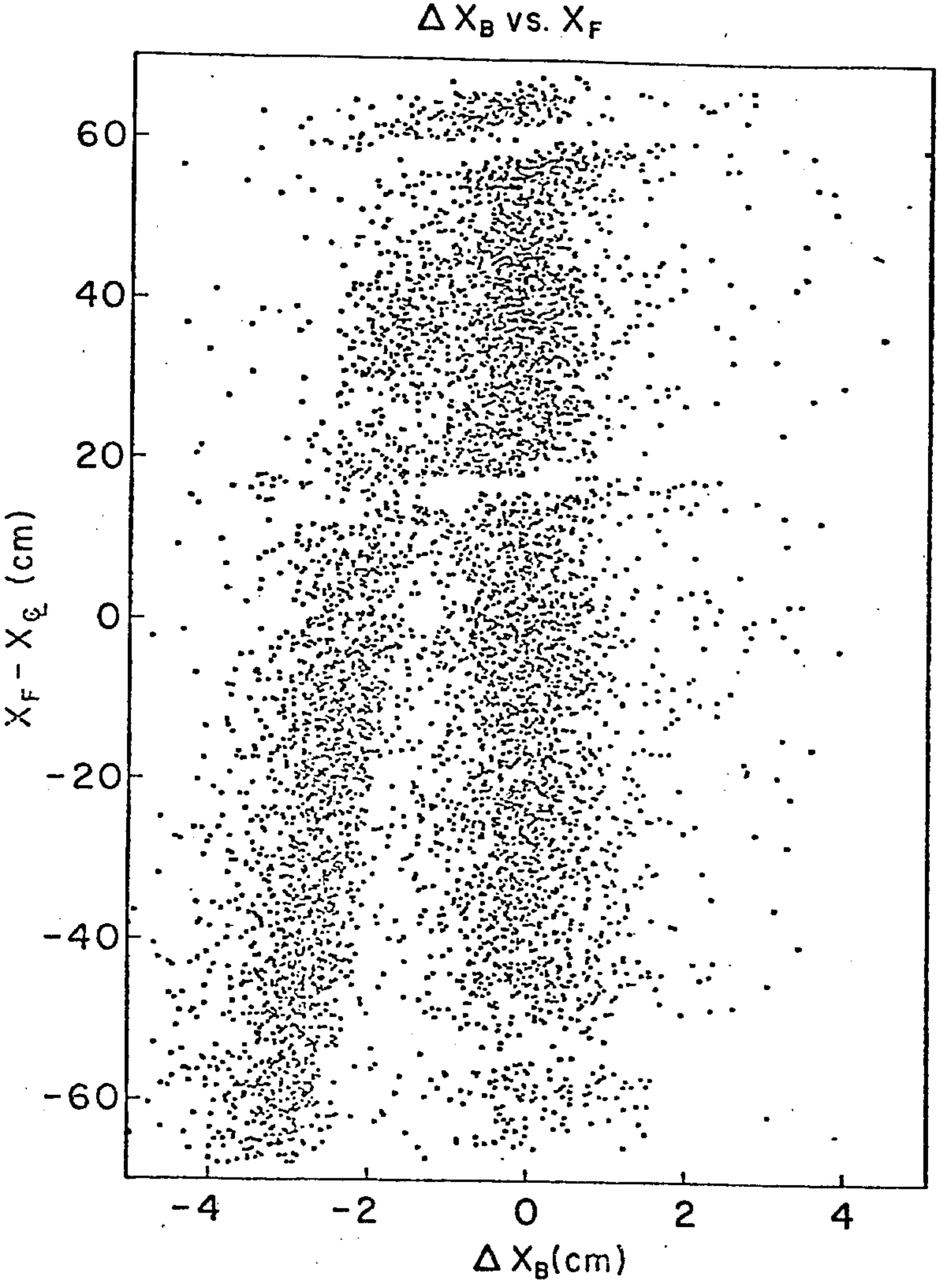
ΔX_B vs. X_F
60
40
20
0
-20
-40
-60
$X_F - X_{\mathrm{C}}$ (cm)
-4
-2
0
2
4
ΔX_B(cm)

Fig. 13

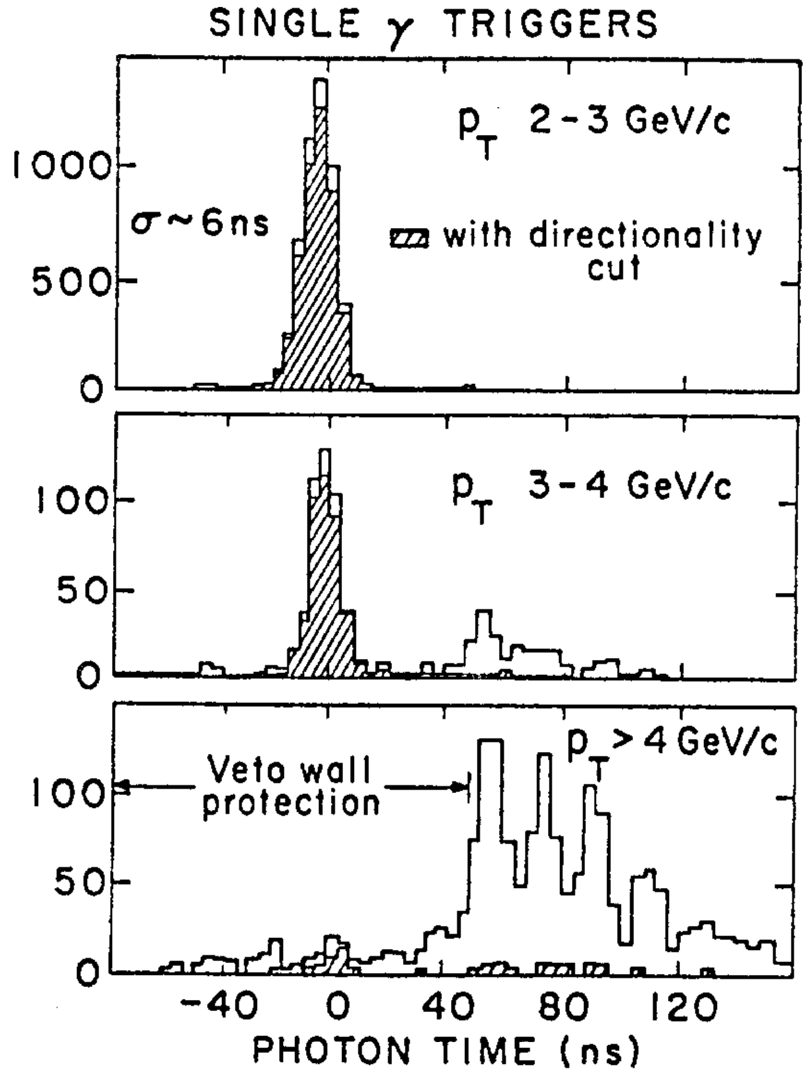
SINGLE γ TRIGGERS
p_T 2-3 GeV/c
1000
$\sigma \sim 6$ns
▨ with directionality cut
500
0
p_T 3-4 GeV/c
100
50
0
$p_T > 4$ GeV/c
Veto wall protection
100
50
0
-40
0
40
80
120
PHOTON TIME (ns)

Fig. 14

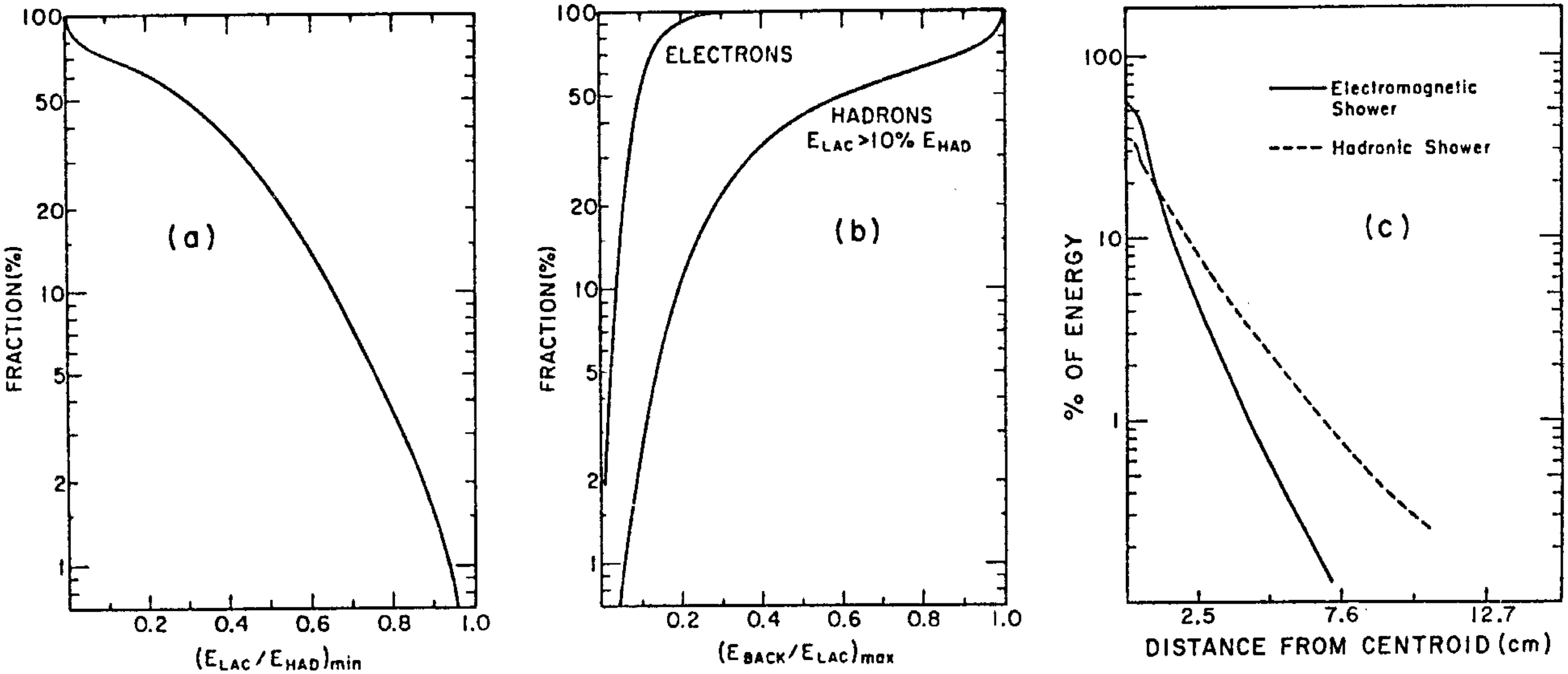(a)
FRACTION(%)
100
50
20
10
5
2
1
0.2
0.4
0.6
0.8
1.0
$(E_{LAC}/E_{HAD})_{min}$
(b)
FRACTION(%)
100
50
20
10
5
2
1
ELECTRONS
HADRONS
$E_{LAC} > 10\% \ E_{HAD}$
0.2
0.4
0.6
0.8
1.0
$(E_{BACK}/E_{LAC})_{max}$
(c)
% OF ENERGY
100
10
1
Electromagnetic Shower
Hadronic Shower
2.5
7.6
12.7
DISTANCE FROM CENTROID (cm)

Fig. 15